

Cite this: *Nanoscale Adv.*, 2022, 4, 3832

Bi₂O₂Se-based integrated multifunctional optoelectronics†

Dharmendra Verma,^a Bo Liu,^b Tsung-Cheng Chen,^a Lain-Jong Li^c and Chao-Sung Lai^{*adef}

The prominent light–matter interaction in 2D materials has become a pivotal research area that involves either an archetypal study of inherent mechanisms to explore such interactions or specific applications to assess the efficacy of such novel phenomena. With scientifically controlled light–matter interactions, various applications have been developed. Here, we report four diverse applications on a single structure utilizing the efficient photoresponse of Bi₂O₂Se with precisely tuned multiple optical wavelengths. First, the Bi₂O₂Se-based device performs the function of optoelectronic memory using UV ($\lambda = 365$ nm, 1.1 mW cm⁻²) for the write-in process with SiO₂ as the charge trapping medium followed by a +1 V bias for read-out. Second, associative learning is mimicked with wavelengths of 525 nm and 635 nm. Third, using similar optical inputs, functions of logic gates “AND”, “OR”, “NAND”, and “NOR” are realized with response current and resistance as outputs. Fourth is the demonstration of a 4 bit binary to the decimal converter using wavelengths of 740 nm (LSB), 595 nm, 490 nm, and 385 nm (MSB) as binary inputs and output response current regarded as equivalent decimal output. Our demonstration is a paradigm for Bi₂O₂Se-based devices to be an integral part of future advanced multifunctional electronic systems.

Received 21st April 2022

Accepted 15th July 2022

DOI: 10.1039/d2na00245k

rsc.li/nanoscale-advances

Introduction

The development of optoelectronic memory (OEM) is one of the key applications that emerged from the novel phenomenon of light–matter interaction (LMI) and has become more crucial due to its merits over conventional resistive memory in terms of data storage and fast processing together with optical sensing. The OEM cell receives the information during the write-in (or programming) process through the exposure of light of appropriate wavelength and subsequently read-out (erasing) of stored information by means of an electrical mechanism. The low voltage requirement for the operation of OEM is advantageous not only in data storage but also in the secured transportation of information. Moreover, OEM further adds enhanced storage capacity through the implementation of multilevel data storage

accomplished by improving the ratio of high resistance state (HRS) and low resistance state (LRS). The optically activated switching in OEM improves bandwidth and overcomes the electrical loss in data transmission.^{1–5} Different materials have been extensively explored to demonstrate optoelectronic memory, such as semiconductor nano materials (0D,⁶ 1D,⁷ 2D⁸), polymers,⁹ organic,^{10,11} and heterostructures of such materials.^{4,12–15} Furthermore, in some studies, phase change materials have been used to demonstrate optoelectronic memory.^{16,17} Charge trapping plays a vital role in the implementation of optical memory. The charge trapping characteristics of graphene and MoS₂ were studied by graphene/hBN/MoS₂ structures showing different hysteresis curves with variations in the thickness of MoS₂ layers.¹⁸ A single-layer MoS₂-based photonic memory device has been used both for optical sensing and channel materials, and AuNPs are used as charge trapping layers.¹⁹ The OEM proof of concept has been explained by incorporating three distinct 2D materials CuIn₇Se₁₁, InSe, and MoS₂ via trapping and releasing photogenerated charge carriers with the gating effect. Additionally, an array of such devices that resembles conventional charge-coupled devices (CCDs) for image sensors was studied.²⁰ The photoresponsive properties of the hybrid structure of graphene and MoS₂ are used to realize optoelectronic memory. However, the high electrical conductivity of graphene yields a high dark current and hence a low ON/OFF ratio (<2) and is a challenge for the success of the structure.²¹ Functionalization of the MoS₂/dielectric interface produces an artificially structured charge trap layer that is used

^aDepartment of Electronic Engineering, Chang-Gung University, Taoyuan 33302, Taiwan. E-mail: cslai@mail.cgu.edu.tw; Tel: +886-3-2118800 ext. 5786

^bFaculty of Information Technology, College of Microelectronics, Beijing University of Technology, Beijing 100124, People's Republic of China

^cDepartment of Mechanical Engineering, University of Hong Kong, Pokfulam Road, 999077, Hong Kong

^dDepartment of Nephrology, Chang Gung Memorial Hospital, Linkou, 33302, Taiwan

^eDepartment of Materials Engineering, Ming-Chi University of Technology, New Taipei City 24301, Taiwan

^fArtificial Intelligence Research Center, Chang Gung University, Taoyuan 33302, Taiwan

† Electronic supplementary information (ESI) available. See <https://doi.org/10.1039/d2na00245k>



to implement monolayer MoS₂-based optoelectronic memory with an improved ON/OFF ratio (4700) and a long storage lifetime (10⁴ s).²² In recent studies, Alexey Lipatov *et al.* have reported an improved ON/OFF ratio (10⁵) with (ON state) and without (OFF state) light illumination over MoS₂-Pb (Zr, Ti) O₃ structure for optical memory.²³ Feng Gao *et al.* reported a multibit optical memory with low optical power (0.32 nW) based on the SnS₂/h-BN/graphene structure.¹⁵ Among recent reports, Yuqian Chen *et al.* demonstrated a heterostructure of PtS₂/h-BN/graphene as multibit optoelectronic memory, which performed up to 74 differentiable states (>6 bits) *via* controlled linear conductance using light pulses.²⁴

In concern with multifunction, specific operations are also performed within the memory devices such as arithmetical operation,^{1,25} logic operation (function of digital logic gates: “AND”, “OR”, “NAND”, “NOR”),^{2,16,26–28} and Pavlovian associative learning process.^{29–31} Moreover, photomemristers^{28,32,33} and photonic synapse³⁴ were also studied and reported. Although substantial efforts and success have been reported, optoelectronic memory devices with multifunction operation by new materials/structures are in everlasting demand. Bi₂O₂Se, a new layered 2D material, has been paid much attention during the last half decade because of its ultra-high mobility (>20 000 cm² V⁻¹ s⁻¹ at 2 K), vigorous band gap (1.9 eV for monolayer), and excellent air stability showing enough potential of exceeding 2D materials.³⁵ Compared to other van der Waals 2D materials, Bi₂O₂Se is composed of alternated stacked layers of Bi₂O₂²⁺ and Se²⁻ layers interacting with weakly electrostatic forces. Competent light absorption property and moderate band gap (~0.8 eV) make Bi₂O₂Se a favorable material for optoelectronic applications.^{36–38} Major reported synthesis methods are CVD,³⁵ wet chemical process,³⁹ precursor co-evaporation,⁴⁰ hydrothermal process,^{41,42} solution assisted method,⁴³ and organic-CVD.⁴⁴ Significant efforts have been made in the synthesis of Bi₂O₂Se to improve the grain size to make it more applicable. The major reports regarding grain size include micrometer (>200 μm),³⁵ millimeter,⁴⁵ and wafer scale size.⁴⁷ Along with optical property, Bi₂O₂Se also represents ferroelectric/ferroelastic property,⁴⁸ inherent bolometric effect,⁴⁹ and phase transition under compression (30 GPa).⁵⁰ Among various properties of Bi₂O₂Se, optical sensing has been widely explored in the development of phototransistors^{45,47,51,52} and photodetectors.^{49,53} In other recent reports, Bi₂O₂Se has been found in vast fields of applications: transistor,^{54,55} polymer solar cell,⁵⁶ broad band photodetector (IR to THz),⁵⁷ coincidence detection,⁵⁸ and memristors.⁵⁹ Wu *et al.* have explored high electron mobility and quantum oscillations in layered Bi₂O₂Se and fabrication of top gate FET showing ON/OFF ratio >10⁶ and subthreshold swing 65 mV per decade (at room temperature) with Hall mobility 450 cm² V⁻¹ s⁻¹.⁶⁰ The heterostructure of Bi₂O₂Se/graphene was reported for the demonstration of photodetector and short channel FET (50 nm) by Tan *et al.*⁶¹ In another study by Yang *et al.*, Bi₂O₂Se/graphene hybrid structure was utilized to demonstrate multifunctional optoelectronics, including photodetector, optical synapse, and logic gate by the control of optical wavelengths.⁶² Some recent reports focused on Bi₂O₂Se-based heterostructures: Bi₂O₂Se/Bi₂Se₃,⁶³ Bi₂Te₂Se/

Bi₂O₂Se,⁶⁴ Bi₂O₂Se/TMDs,⁶⁵ and Bi₂O₂Se/CsPbBr₃,⁶⁶ showing potential use of Bi₂O₂Se in combination with other materials for optoelectronic applications. Although Bi₂O₂Se shows competent light sensing property in a wide band, multifunctional optoelectronic by only the Bi₂O₂Se based structure has not been explored so far.

In this report, we explore the spectacular light sensing characteristic of Bi₂O₂Se by the implementation of four distinct applications, namely optoelectronic memory, associative learning process, digital logic, and 4 bit binary to the decimal converter by means of precisely tuned multiple optical wavelengths over a single Bi₂O₂Se based structure. The generation of photonic charge carriers under exposure of UV ($\lambda = 365$ nm, 1.1 mW cm⁻²) and trapping/detrapping of these charge carriers *via* bias potential reveals the operation of OEM. The effect of exposure dose, optical power density, and waiting time over the performance are also investigated. Next, the associative learning process is demonstrated by considering the drooling of a dog as an example. The wavelengths 635 nm (2.0 mW cm⁻²) and 525 nm (2.0 mW cm⁻²) were adopted as neutral stimuli (NS) and unconditional stimuli (US), respectively, while the level of output current determines the behavioral change of the dog. We further realize the function of logic gates by utilizing the same wavelengths as digital inputs while the response current level shows the output for “AND” and “OR” gates, and the corresponding resistance level shows the output for “NAND”, and “NOR” gates. The implementation of a 4 bit binary to decimal converter is proposed and realized for the first time. The operation is accomplished by considering four different wavelengths 740 nm (LSB), 595 nm, 490, and 385 nm (MSB) as binary inputs (from “0000” to “1111”) while the response current is regarded as equivalent decimal output (from “0” to “15”). Our demonstration evidences a single Bi₂O₂Se based structure having enough ability to perform multiple optoelectronic functions.

Results and discussion

The Bi₂O₂Se nanoplates were synthesized over a MICA substrate *via* a well-accepted low-pressure chemical vapor deposition (LPCVD) method using Bi₂O₃ and Bi₂Se₃ as precursor materials and Ar as the carrier gas with a pressure condition of 100 torr. Later, the synthesized Bi₂O₂Se nanoplates were transferred to a SiO₂/Si substrate (for device fabrication) by PMMA, PDMS sheets, and a water assisted method (details are available in the Experimental section).⁶⁷ Fig. 1a shows a schematic view of the layered structure of Bi₂O₂Se with a color difference for constituent atoms where gray balls are Se, red balls are O, and pink balls are Bi. The schematic represents four layers with a total thickness of 24.32 Å. The thickness of the monolayer Bi₂O₂Se is 6.08 Å.³⁵ The lateral gap between two successive Se atoms is 3.88 Å. Raman spectroscopy (Fig. 1b) was carried out for as-grown Bi₂O₂Se nanoplates over the MICA substrate, displaying a major peak $A_{1g}^2 = 158$ cm⁻¹, which confirms the growth of the Bi₂O₂Se material, consistent with previous reports.^{35,45} Two other peaks with comparatively low intensities observed at 217 and 233 cm⁻¹ due to out-of-plane vibrations of “O” atoms are associated with α -Bi₂O₃ and β -Bi₂O₃ phases, respectively.⁴⁶ The



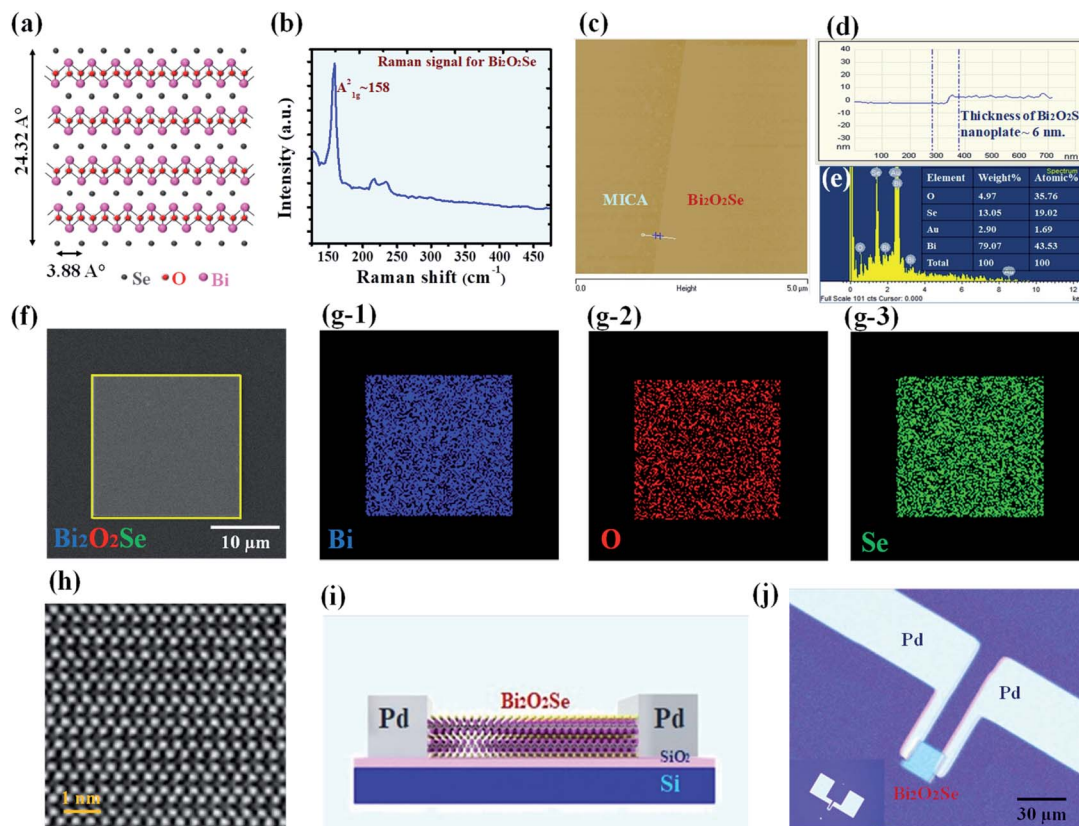


Fig. 1 $\text{Bi}_2\text{O}_2\text{Se}$ material characterization and device fabrication. (a) A schematic view of the layered crystal structure of $\text{Bi}_2\text{O}_2\text{Se}$ (representing four layers with gray, red, and pink balls for “Se”, “O”, and “Bi” respectively). (b) Raman spectroscopy of the $\text{Bi}_2\text{O}_2\text{Se}$ nanoplate using a 532 nm laser ($A_{1g}^2 = 158 \text{ cm}^{-1}$). (c) AFM analysis of the $\text{Bi}_2\text{O}_2\text{Se}$ nanoplate as grown over the MICA substrate, and (d) thickness measured $\sim 6 \text{ nm}$ (~ 9 layers). (e) EDS spectra representing compositional elements: Bi, O, and Se of $\text{Bi}_2\text{O}_2\text{Se}$ with additional peaks for Si (substrate) and Au (2 nm coating for surface modification). (f) Electron image of the $\text{Bi}_2\text{O}_2\text{Se}$ nanoplate and corresponding elemental maps for Bi (g-1), O (g-2), and Se (g-3). (h) Cross-sectional HRTEM image of $\text{Bi}_2\text{O}_2\text{Se}$ with a scale bar 1 nm. (i) Schematic view of the $\text{Bi}_2\text{O}_2\text{Se}$ based device. (j) OM image of top view of fabricated device with Pd as metal contact on SiO_2/Si (inset: full top view of structure).

atomic force microscopy (AFM) analysis of $\text{Bi}_2\text{O}_2\text{Se}$ nanoplates (Fig. 1c) shows that the thickness of $\text{Bi}_2\text{O}_2\text{Se}$ was $\sim 6 \text{ nm}$ (Fig. 1d), revealing the number of layers ~ 9 (monolayer thickness of $\text{Bi}_2\text{O}_2\text{Se} = 0.608 \text{ nm}$). Fig. 1e represents the presence of constituent elements “Bi”, “O”, and “Se” confirmed by EDS spectra in view of the corresponding peaks. There are some other peaks for Si (substrate) and Au (to make the surface conductive for FESEM analysis). The elemental weight and atomic percentage are added in the inset. EDS mapping confirms the qualitative chemical composition of $\text{Bi}_2\text{O}_2\text{Se}$ nanoplate, electron image (Fig. 1f with the area selected for EDS mapping shown in yellow color), and corresponding elemental mapping images showing the uniform distribution of “Bi” (Fig. 1g-1), “O” (Fig. 1g-2), “Se” (Fig. 1g-3) elements. The dimensions (length & width) of the $\text{Bi}_2\text{O}_2\text{Se}$ nanoplate were measured to be $22 \mu\text{m}$ and $22 \mu\text{m}$, respectively, which shows that the $\text{Bi}_2\text{O}_2\text{Se}$ nanoplate was almost square in shape. The $\text{Bi}_2\text{O}_2\text{Se}$ surface was observed without any processing residue over it, indicating its suitability for device fabrication. Fig. 1h shows high-resolution transmission electron microscopy (HRTEM) image of the $\text{Bi}_2\text{O}_2\text{Se}$ lattice, which confirms high crystallinity in structure and resembles the theoretical

depiction. A schematic diagram of the device structure is shown in Fig. 1i. The $\text{Bi}_2\text{O}_2\text{Se}$ -based device was fabricated with palladium (Pd) as the metal contact and p + Si as the back gate electrode. For the back gate metal contact, aluminum (Al) was used (not shown in the figure). The OM image of the top view of the fabricated device (inset shows the complete view of the device) is presented in Fig. 1j.

Optoelectronic memory

The $\text{Bi}_2\text{O}_2\text{Se}$ -based device is first utilized to demonstrate the operation of optoelectronic memory.^{19–22} The operating principle of optoelectronic memory is based on the trapping of charge (preferably electrons) generated by controlled optical power and the subsequent detrapping of charge upon application of bias voltage. The complete function of optoelectronic memory includes three major steps: first is the trapping of photogenerated charge (regarded as storing the information, writing: optical method), second is the waiting time (WT: the time during which the charge remains trapped or information retention period: electrical method, by applying back gate bias), and third is the detrapping of charge (regarded as the extraction of information, reading: electrical method, by applying a voltage



between the source and drain). A material with the ability to generate electron–hole pairs by absorbing energy from photo-excitation is termed a photoactive material (the active layer within a device) and is the core unit of optoelectronic memory. The material used to trap such photonically produced charge is termed as trapping material (the trapping layer within a device) and is the second key unit of optoelectronic memory. The active layer can also function as a trapping layer.^{20,22} In our structure, Bi₂O₂Se has been considered an active layer, while SiO₂ beneath Bi₂O₂Se is considered a trapping layer. Since Bi₂O₂Se shows a good photoresponse,^{45,51} its selection as an active layer in the structure of optoelectronic memory is reasonable, while the presence of trapping sites (due to dangling bonds)⁶⁸ over the surface of SiO₂ makes it suitable for charge trapping medium.

Fig. 2(a)–(c) depicts the energy band diagram (with Schottky barrier profile) to explain the mechanism of optoelectronic memory involving charge trapping, WT, and detrapping of charge. A potential of +10 V is applied on the back gate throughout the process. This potential helps in the formation of potential wells in the trapping layer. During write-in, a UV light was applied over the device. The photons of the light pulse absorbed by the active layer (Bi₂O₂Se) generate a number of electron–hole (e–h) pairs. These photonically generated electrons become trapped in the trapping sites (between Schottky barriers ϕ_{b1} and ϕ_{b2}) available at the Bi₂O₂Se/SiO₂ interface,⁶⁸ while holes move through the Schottky barrier between the metal (Pd) semiconductor interface (ϕ_{b1} and ϕ_{b2}) available on both sides (Fig. 2a). After that, the device was held in a sufficiently dark condition with an applied back gate bias. The trapped electrons (on the surface of the SiO₂ interface) remain over a span of time known as WT, which represents the storage

of information (Fig. 2b). Moreover, this WT is a significant parameter for both data and image processing in real time.²⁰ After completion of the WT, a read-out bias (+1 V) is applied (between end point terminals S/D). Due to this read-out bias, the Schottky barrier on one side (ϕ_{b2}) becomes reverse biased (preventing leakage of charge or loss of information), while the other Schottky barrier (ϕ_{b1}) turns in the forward bias condition. The forward biased Schottky barrier (ϕ_{b1}) lowers the barrier height and allows the trapped electrons to move out (Fig. 2c). This step in which the trapped electrons are released is termed as read-out or receiving of stored information. The response current obtained by these electrons is regarded as the reading of information, which is the last step in the function of optoelectronic memory.

The response current inherently depends upon the optical power density (OPD) and exposure dose (ED: exposure duration) of the applied optical wavelength. The WT also has a significant influence on the response (or reading) current. These parameters affecting the reading current are explained in the following section.

To demonstrate the optoelectronics memory process by using a Bi₂O₂Se-based device, first, the selection of an appropriate optical wavelength was made by measuring the device (under fixed terminal voltage $V_{ds} = 1$ V, and varying back gate voltage V_{bg} from -20 V to $+40$ V) response current in the dark and under exposure to optical wavelengths of 635 nm, 460 nm, and 365 nm as shown in Fig. 3a. The OPD for each wavelength was 1.1 mW cm⁻². This measurement shows the optical wavelength of 365 nm (ultraviolet) causes a higher response current. The photo to dark current ratio (PDCR = I_{ph}/I_{dark} , where $I_{ph} = I_{illumination} - I_{dark}$)⁶² for wavelengths 635 nm, 460 nm, and 365 nm

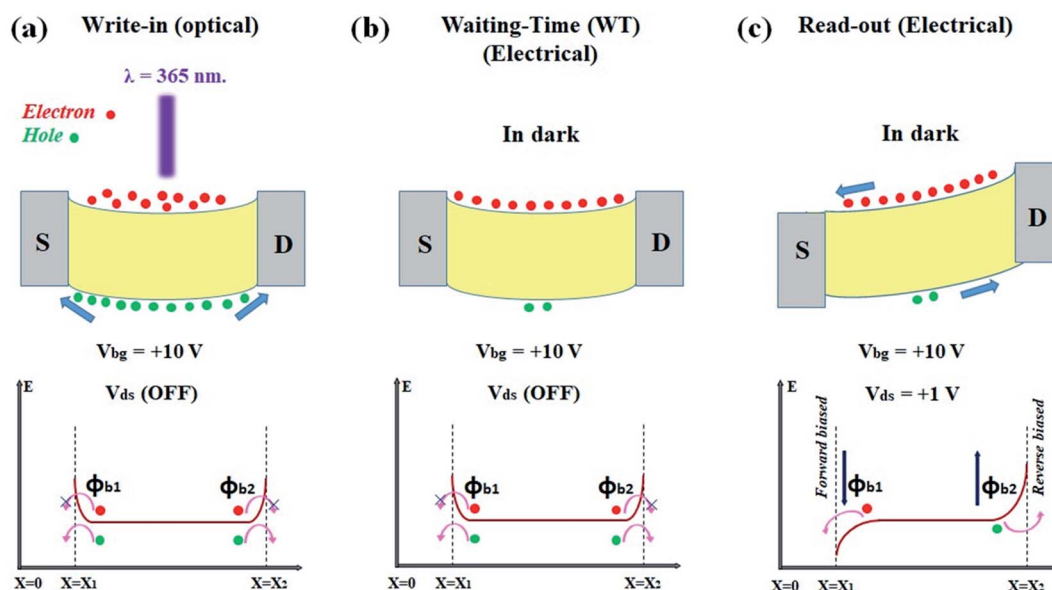


Fig. 2 Energy band diagram (with Schottky barrier profile) representing the mechanism of optoelectronic memory process. (a) After UV illumination, trapping of electrons (at the surface of the trapping layer-SiO₂) within Schottky barriers (ϕ_{b1} and ϕ_{b2}) formed at metal (Pd) and semiconductor interfaces, while holes move through any of the Schottky junction. (b) The electrons remain trapped (due Schottky barriers ϕ_{b1} and ϕ_{b2}) over the duration of time termed as waiting time (charge storage time). (c) A read-out bias +1 V (with $V_{bg} = +10$ V) leads the Schottky barrier to drop down on one side (ϕ_{b1}) releasing the trapped electrons, which is termed as read-out of the information.



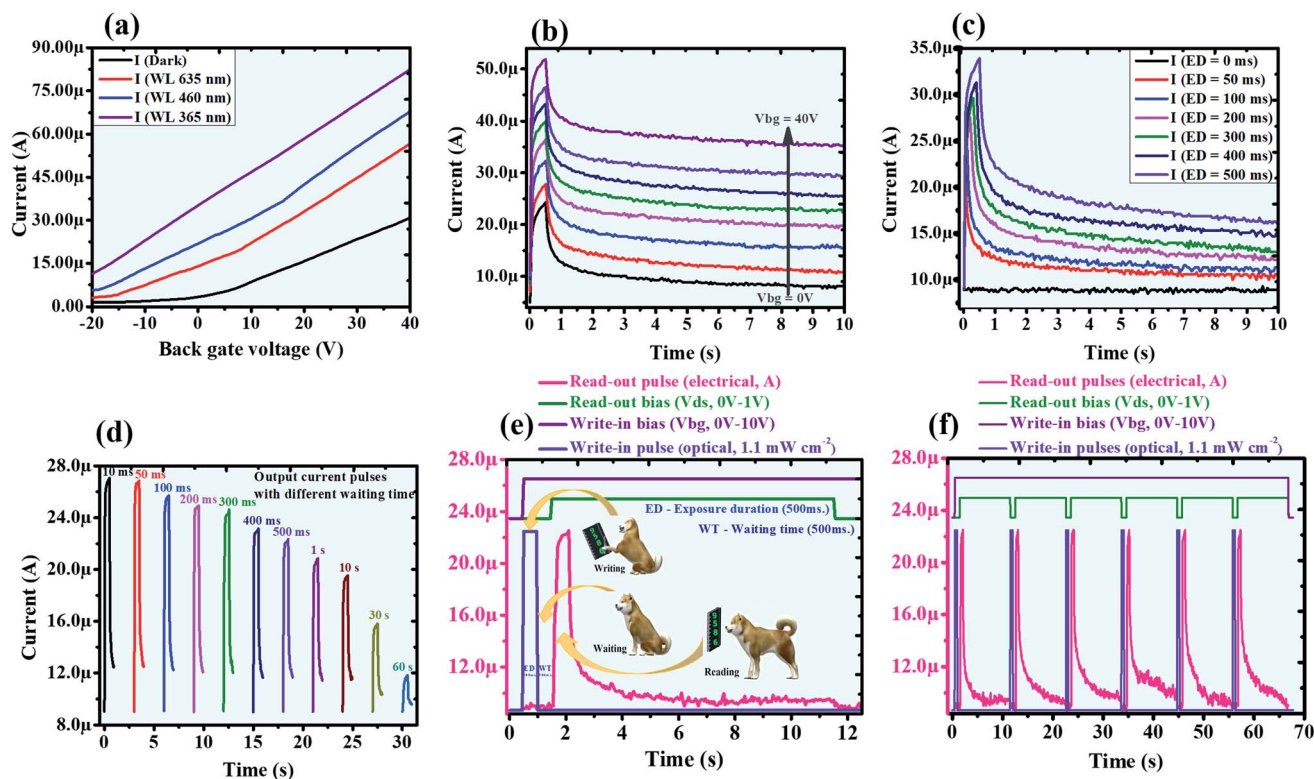


Fig. 3 Bi₂O₂Se based optoelectronic memory. (a) Variation in device response current in the dark and under exposure with different wavelengths 635 nm, 460 nm, and 365 nm with back gate voltage (applied $V_{ds} = +1$ V). (b) Effect of back gate voltage (0 V to 40 V) on the response current when using UV exposure (365 nm power density 1.1 mW cm^{-2} , duration 500 ms). (c) The significant effect of exposure dose on the response current. The peak response current increases when exposure dose increases from 0 ms, to 500 ms. (d) The peak response current was observed to decrease while waiting time continues to increase. (e) Write–Wait–Read process for first single pulse application. Write process is done by applying optical pulse (365 nm, power density 1.1 mW cm^{-2} , exposure duration 500 ms) with back gate voltage $+10$ V. After waiting time of 500 ms, a read out bias $+1$ V is applied between the source and drain to extract the information as read out current. (f) Six consecutive Write–Wait–Read (WWR) operation proving the successful realization of optoelectronics memory process.

was 1.579, 2.571, and 4.464, respectively (Fig. S1†). Since the optical wavelength of 365 nm showed the highest PDCR, it can generate an adequate number of photonic charges (e–h pairs), so this UV light was selected for exposure throughout the demonstration of the optoelectronic memory process. Next, the effect of the back gate voltage on the response current for a duration of 10 s was measured (Fig. 3b) for exposure with an OPD of 1.1 mW cm^{-2} and a duration of 500 ms. The terminal voltage (V_{ds}) was 1 V while the back gate voltage V_{bg} was selected from 0 V to 40 V. The values applied for the back gate voltage were 0, 5, 10, 15, 20, 25, 30, 40 V, and the corresponding peak values of the response current were 24.3, 27.8, 32.3, 36.4, 39.9, 43.2, 46.5, and $51.9 \mu\text{A}$, respectively (Fig. S2†). The measurements show that the effect of the back gate voltage not only increases the peak value of the response current but also improves the decay of the response current over time. The slow decay of the response current indicates the storage of photonic charge over more time, which improves the WT of optoelectronic memory. The bolometric effect has been observed with Bi₂O₂Se due to thermal heat caused by optical incident power.⁶² This effect is found both with and without back gate voltage. We observed that the photoconductive effect

without a back gate voltage shows a current of $250 \mu\text{A s}^{-1}$ and a bolometric effect with a current of $6.8 \mu\text{A s}^{-1}$, while with a back gate voltage, the photoconductive effect shows a current of $680 \mu\text{A s}^{-1}$ and a bolometric effect with a current of $5.4 \mu\text{A s}^{-1}$. This shows that the back gate voltage increases the photoconductive effect while slowing the current in the region of the bolometric effect. This is due to leakage of charge causing a gate current when a higher back gate voltage is applied, and hence, the total charge that needs to be contributed to the bolometric effect is reduced, resulting in a slowdown of the current in the region of the bolometric effect (Fig. S3†). The leakage of charge (stored information) in the form of gate current increases with gate voltage at higher values. The leakage of charge needs to be avoided to retain the stored information over time. Fig. S4† shows gate currents of 0.4, 2, 9, 20, 36, 60, 86, and 155 pA with applied back gate voltages of 0, 5, 10, 15, 20, 25, 30, and 40 V. To prevent loss of information and to demonstrate the optical memory process with maximum charge storage (information writing) and minimum charge leakage (information loss), the selected value of the back gate voltage was 10 V. With this value of the back gate voltage, we measured the peak value of charge and then the value of charge after 10 s of decay



as shown in Fig. S5.† We observed that the amount of charge with $V_{bg} = 10$ V ($q \sim 7.2 \times 10^{-7}$ C) was significantly higher than the charge at $V_{bg} = 0$ V ($q \sim 5.4 \times 10^{-7}$ C). After 10 s, the remaining amount of charge with $V_{bg} = 10$ V and 0 V were $\sim 3.8 \times 10^{-7}$ C and $\sim 1.8 \times 10^{-7}$ C, respectively. This inferred that the selection of $V_{bg} = 10$ V is pertinent for the demonstration of the optoelectronic memory process. The OPD is one of the responsible parameters for the generation of photonic charge. Fig. S6† shows the amount of photonic charge generated with different levels of OPD. The plot indicates that the amount of photonic charge increases at a much higher rate at initial values of OPD (~ 1 mW cm $^{-2}$), while the incremental rate of photonic charge becomes slower as the OPD increases to higher values (>1.1 mW cm $^{-2}$). We found an OPD of 1.1 mW cm $^{-2}$ to be appropriate for exposure by observing the plotted numerical values in Fig. S6.† After observing the effects of OPD, we measured the effect of exposure duration (ED), as shown in Fig. 3c. It was found that as the ED increases, the peak response current also increases.²⁰ As the ED was increased to values of 0, 50, 100, 200, 300, 400, and 500 ms, the response current values were measured to be 8.9, 23, 24.75, 27.55, 29.6, 31.3, and 33.9 μ A, respectively. With this measurement, we selected an ED of 500 ms. Fig. S7† shows that the peak amount of photonic charge increases as the exposure dose increases. During the measurement of the effect of ED on the response current (or photonic charge), we also closely observed the dependency of the bolometric effect on ED. Fig. S8† shows that when the ED was 50 ms, the bolometric effect was less significant, and when the ED was increased to 500 ms, the bolometric effect became prominent. This is because more thermal heat caused by boosting the ED leads to the effective appearance of bolometric effects. The WT is another key parameter that governs the performance of optoelectronic memory. To analyze the effect of WT on the response current, we used an exposure by a 365 nm laser with an OPD of 1.1 mW cm $^{-2}$ and an ED of 500 ms, as these were the preselected parameters. The applied voltages V_{ds} and V_{bg} were 1 V and 10 V, respectively. Fig. 3d represents the pulses of the output response current having different peak values because they acquired different WTs. This bears out the downward trend of the response current with increasing WT. The major factor responsible for the decay of the peak response current is the leakage of charge through the trapping layer (SiO $_2$) due to the applied back gate voltage. To avoid such leakage of charge, we apply a comparatively lower value of back gate voltage, as discussed earlier (Fig. S4†). More WT causes more leakage of charge that leads to the loss of information. Fig. S9† represents the decay of charge with respect to different WTs. When the WT was small (<1 s), the decay of charge was observed to be slow, and when the WT was increased (>1 s), the charge decayed at a much faster rate. With this measurement, we selected a WT of 500 ms (<1 s) for the demonstration of optoelectronic memory. Furthermore, the variation in the ON/OFF ratio with parameters such as back gate voltage (V_{bg}), ED, WT, and OPD for the present optoelectronic memory device was determined and is presented in Fig. S10.†

Fig. 3e represents one complete step of the write–wait–read (WWR) process, elaborating the function of optoelectronic

memory. First, an optical pulse was applied as a write-in pulse ($\lambda = 365$ nm, OPD = 1.1 mW cm $^{-2}$, ED = 500 ms). This optical pulse causes the generation of e–h pairs by the active layer, out of which electrons become trapped at the interface of Bi $_2$ O $_2$ Se/SiO $_2$. After the write-in pulse, a WT of 500 ms was taken into account with $V_{bg} = +10$ V and $V_{ds} = 0$ V. Upon completion of the WT, a read-out bias $V_{ds} = +1$ V was applied along with $V_{bg} = +10$ V. A response current pulse (~ 22.5 μ A) was measured and regarded as a read-out pulse. It is quite interesting that the duration of the read-out pulse (electrical current) is approximately 500 ms, which is equal to the duration of the applied optical write-in pulse. The output response current decreases and reaches its previous level when V_{ds} reaches 0 V again after a duration of 10 s. To confirm our implementation, we repeated the write–wait–read (WWR) steps six consecutive times (including the first pulse shown in Fig. 3e), as represented in Fig. 3f. The exposure wavelength, OPD, and ED were 365 nm, 1.1 mW cm $^{-2}$, and 500 ms, respectively, while the write-in bias (V_{bg}) was +10 V and the read-in bias (V_{ds}) was +1 V. All the associated parameters, including WT (500 ms), were kept invariant for each step of the six consecutive cycles of the WWR process. The read-out current pulse level was observed to be ~ 22.5 μ A during each step. The consistency in the read-out current level proves the successful realization of the optoelectronic memory function utilizing a Bi $_2$ O $_2$ Se-based device. After each read-out bias, the output current reverts to its original level (dark current level) by showing some relaxation with little difference each time. This was mainly observed under low current levels. The possible factors for such behavior are excess stored charge²² or substrate surface effects. Although these effects may lead to further studies relating to performance improvement of the device, such effects were observed to be less significant at the peak level of the output response current; hence, we did not pay much attention to such effects quantitatively in our present study. Additionally, we have completed measurements of optoelectronic memory in a dark environment at room temperature while ignoring the other influencing factors of the signal-to-noise (S/N) ratio and the effect of thermal excitations,²⁰ as such effects are more crucial with low current level (pA). A brief comparison with major reported references on optoelectronic memory processes based on 2D materials is presented in Table S1.†

With this demonstration, we successfully realized optoelectronic memory using a Bi $_2$ O $_2$ Se-based device. Furthermore, making such devices integral parts of an array leads to the development of image sensors in which one device will represent one pixel. Moreover, the ability to gather information from illumination vindicates the application of such Bi $_2$ O $_2$ Se-based devices in the development of artificial eyes.

Associative learning process

One of the important key aspects of the learning process is conditioned learning, also known as the associative learning process.^{29–31,69} This conditioned learning process is accomplished using an unconditioned stimulus (US) in association with a neutral stimulus (NS) to alter the behavioral response



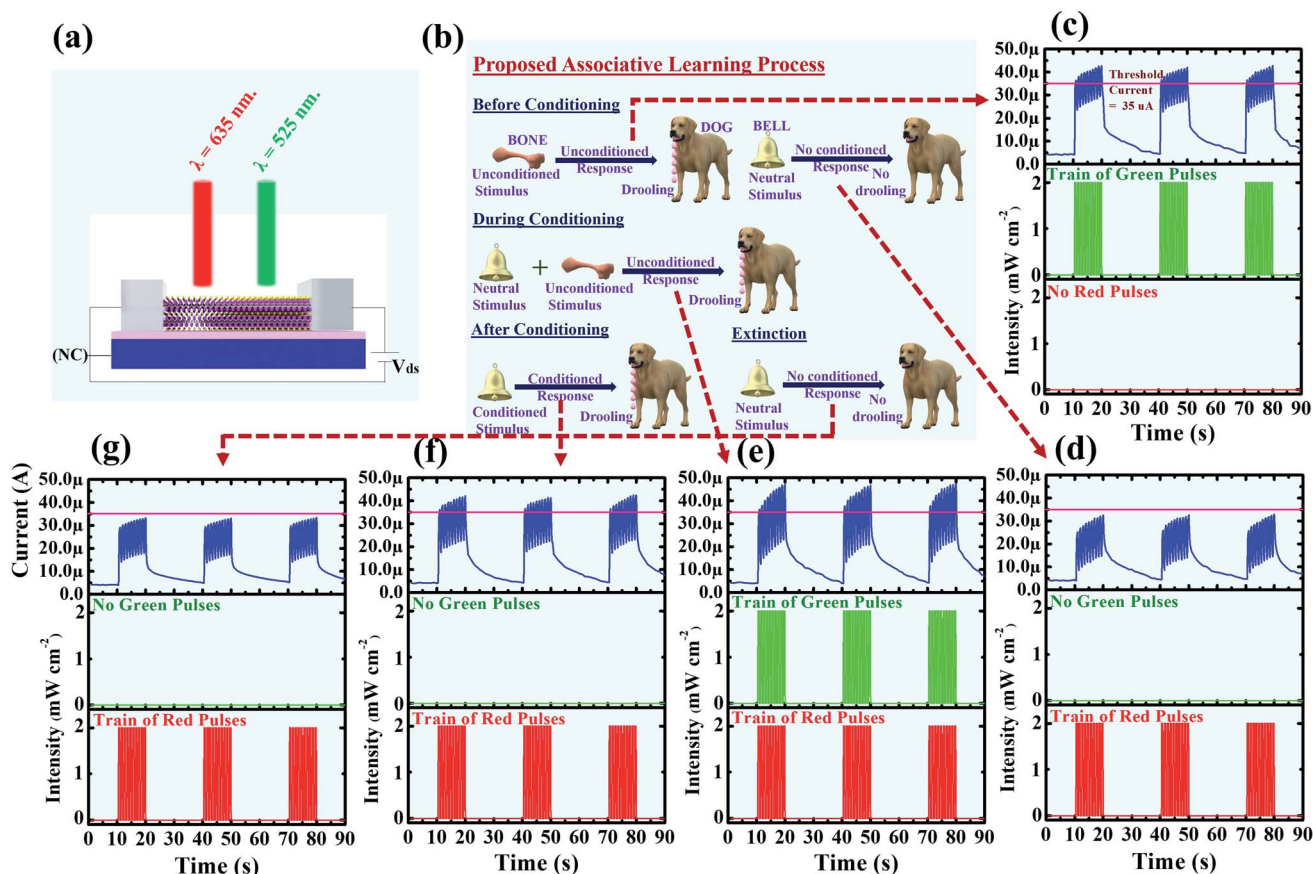


Fig. 4 Mimicking associative learning process. (a) Schematic of device structure with exposure of optical wavelengths 525 nm and 635 nm. (b) Proposed associative learning process showing unconditioned and conditioned response (conditioned learning) by the dog followed by extinction (forgetting). (c) Unconditioned response (on application of 525 nm before conditioning). (d) No conditioned response (on application of 635 nm before conditioning). (e) Unconditioned response (on application of 525 nm + 635 nm during conditioning). (f) Conditioned response (on application of 635 nm only after conditioning). (g) Extinction (on application of 635 nm only, after 90 s of conditioning).

into a conditioned response (CR). The proposed conditioned learning process is that of a dog drooling when offered a piece of bone as food (Fig. 4b). Before conditioning, the dog drools (unconditioned response- UR) by seeing piece of bone (US) and does not drool (no conditioned response- NCR) by ringing the bell (NS) only. During conditioning, the dog drools (UR) when seeing piece of bone (US) associated with ringing bells (NS). After conditioning, the dog shows drooling (CR) with a ringing bell (CS) only. This infers that the neutral stimulus (ringing bell) shows no conditioned response and has become a conditioned stimulus (CS) showing a conditioned response (CR). An extinction represents the resumption of previous behavior by CS \rightarrow NS with CR \rightarrow no response, which is also termed as forgetting. To demonstrate the proposed conditioned learning process, an optical input wavelength of 635 nm was used as neutral stimulus (NS), and 525 nm was used as unconditioned stimulus (US) with the present Bi₂O₂Se device (Fig. 4a). The optical input pulse period was 500 ms with a power density of 2.0 mW cm⁻². The output response current was considered the indicator of behavioral change (of the dog) with a threshold current level of 35 μ A for the present device. When the current level is higher than the threshold for any optical input, the dog's

behavior is assumed to be "drooling", and when the current level is lower than the threshold, the dog's behavior is assumed to be "no drooling". Before conditioning, groups of 10 consecutive pulses of wavelength 525 nm were used. It (US) was applied three times, and the output current was 42.6 μ A, higher than the threshold level (35 μ A), causing an unconditioned response (UR-drooling) (Fig. 4c). Ten consecutive pulses of wavelength 635 nm (NS) were applied three times, and the output current was observed to be 32.5 μ A, lower than the threshold level (35 μ A), showing no conditioned response (NR-no drooling) (Fig. 4d). During conditioning, the optical wavelength of 525 nm was applied associated with wavelength 635 nm (US + NS) in three groups of 10 consecutive pulses. The output response current was observed to be 47.0 μ A, higher than the threshold (35 μ A), showing an unconditioned response (UR-drooling) (Fig. 4e). After conditioning, 10 consecutive pulses of wavelength 635 nm were applied three times, and the output current was observed to be 42.1 μ A, higher than the threshold level (35 μ A), showing a conditioned response (CR-drooling) (Fig. 4f). Hence, the wavelength 635 nm became a conditioned stimuli (CS) that caused no response behavior (no drooling) of the dog to be altered into conditioned response (drooling as



conditioned learning). This conditioned response did not remain over a long period of time, and after 90 seconds, an extinction behavior was observed by applying 10 consecutive pulses of 635 nm wavelength three times. The output current was 33.3 μA , lower than the threshold level (35 μA), and thus showed no conditioned response (NR-no drooling). This emulates “forgetting” (Fig. 4g). Therefore, before conditioning, the optical input of 635 nm was a neutral stimulus and became a conditioned stimulus after conditioning (memory). The conditioned stimulus was again converted into neutral stimulus by extinction (forgetting) over a duration of 90 s. The levels of peak currents before conditioning, during conditioning, after conditioning, and extinction are represented in Fig. S11† to show the complete process in one view. Thus, the present device shows the ability to mimic the associative learning process by using all the optical inputs and photoresponse current as output, demonstrating this $\text{Bi}_2\text{O}_2\text{Se}$ device as an optical neuro device with enough capability to show learning/memory and forgetting processes analogous to the biological neurofunction of the human brain.

Digital logic function

In this section, we demonstrate the realization of the basic logic functions “AND”, “OR”, “NAND” and “NOR” by a similar device, as shown in Fig. 5a.^{2,16,26–28} The optical input combinations, input-1 (635 nm) and input-2 (525 nm) with an intensity of 2.0 mW cm^{-2} are regarded as binary inputs (with 525 nm as the

most significant bit MSB, and 635 nm as the least significant bit LSB), while the photoresponse current (I_{out}) is assumed to be the output for “AND” and “OR” logic gates under modulatory back gate voltages (V_{bg}) of 0 V and 10 V, respectively. The output resistance (R_{out}) of the device is assumed to be the output for the “NAND” and “NOR” logic gates (with V_{bg} 0 V and 10 V, respectively). The device characteristics were measured in the dark (with and without back gate voltage, *i.e.*, V_{bg}) and under exposure to light (with and without V_{bg}), as shown in Fig. S12.†

Fig. 5b represents the schematic diagram for the operation of “AND” and “OR” gates. If a particular optical input is “ON”, it represents logical “1”, while optical input “OFF” represents logical “0”. The output represents logical “1” when the output current level (I_{out}) is higher than (or equal to) the threshold value ($I_{\text{th}} = 30 \mu\text{A}$) and “0” when $I_{\text{th}} > I_{\text{out}}$. For the functional realization of the “AND” gate without a back gate voltage ($V_{\text{bg}} = 0 \text{ V}$), the applied optical input combinations are “00”, “01”, “10”, and “11”. The output currents measured are 4.6, 26.2, 28.7, and 31.7 μA , which reveal outputs “0”, “0”, “0” and “1”, respectively (Table 1), proving the logic function for the “AND” gate. For the “OR” gate, a modulatory back gate voltage is applied ($V_{\text{bg}} = 10 \text{ V}$), which lifts up the current level from 4.6 μA to 9.6 μA . With the same threshold value of output current ($I_{\text{th}} = 30 \mu\text{A}$) as the “AND” gate, optical input combinations “00”, “01”, “10”, and “11” are applied, and the output currents measured are 9.6, 35, 36.8, and 39 μA , respectively, corresponding to the outputs “0”, “1”, “1” and “1”, respectively (Table 1), proving the logic function for the “OR” gate.

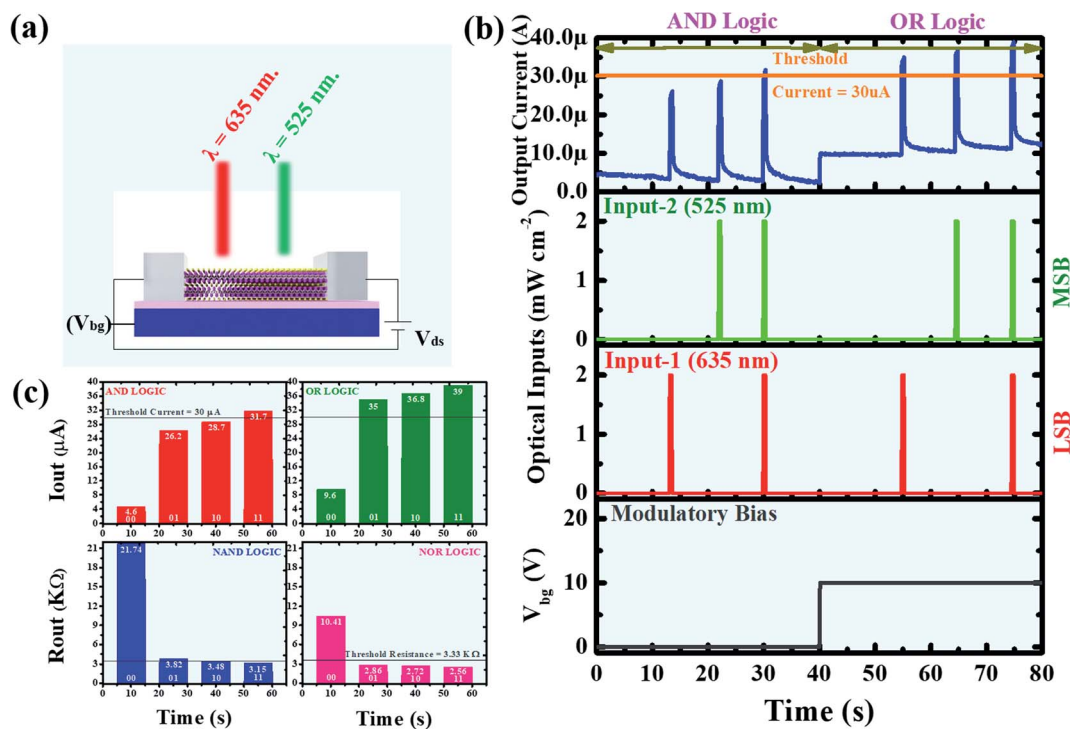


Fig. 5 Realizing the function of digital logic gates. (a) The device under exposure with light 635 nm and 525 nm, as optical binary inputs. (b) Represents device function by logical variation of output current in response of binary optical input combinations for operation of AND gate, and OR gate. (c) Output current level (threshold = 30 μA) reveals AND, and OR logic while the corresponding output resistance (threshold = 3.33 $\text{K}\Omega$) shows NAND and NOR logic.



Table 1 Operational table for AND gate, and OR gate with 2-input binary combinations (optical) and logical output (electrical) showing a high (1) output if output current is higher than threshold (30 μ A) and a low (0) output if output current is lower than threshold

V_{bg} (V)	Logic operation	Input-2 ($\lambda = 525$ nm) green	Input-1 ($\lambda = 635$ nm) red	Output photocurrent (μ A)	Comparison with threshold current I_{th} (30 μ A)	Corresponding logical output
0	AND	0	0	4.6	$4.6 < 30$	0
		0	1	26.2	$26.2 < 30$	0
		1	0	28.7	$28.7 < 30$	0
		1	1	31.7	$31.7 > 30$	1
10	OR	0	0	9.6	$9.6 < 30$	0
		0	1	35	$35 > 30$	1
		1	0	36.8	$36.8 > 30$	1
		1	1	39	$39 > 30$	1

For the “NAND” and “NOR” gates, shown in Fig. 5c, the device output resistance is regarded as the output for the “NAND” and “NOR” gates. For the “NAND” gate, no modulatory voltage is applied ($V_{bg} = 0$ V). The threshold value of the output resistance (R_{th}) is 3.33 K Ω . If the output resistance for a particular input combination is higher than (or equal to) the threshold value ($R_{th} \leq R_{out}$), the output is regarded as logical “1”, and if the output resistance is lower than the threshold value ($R_{th} > R_{out}$), the output is regarded as logical “0”. For the “NAND” gate, the measured output resistances for optical input combinations “00”, “01”, “10”, and “11” are 21.74, 3.82, 3.48, and 3.15 K Ω , respectively, corresponding to outputs “1”, “1”, “1”, and “0” (Table 2), proving the realization of the “NAND” gate. For the “NOR” gate, a modulatory back gate voltage is applied ($V_{bg} = 10$ V). With the same threshold value of output resistance ($R_{th} = 3.33$ K Ω) as the “NAND” gate, optical input combinations “00”, “01”, “10”, and “11” are applied, and the output resistances measured are 10.41, 2.86, 2.72, and 2.56 K Ω , respectively, corresponding to the outputs “1”, “0”, “0” and “0”, respectively (Table 2), showing the logic function of the “NOR” gate.

Therefore, it is clear that the operation of basic logic gates “AND” and “OR” and universal logic gates “NAND” and “NOR” can be realized by tuning optical input combinations and applying modulatory bias. Since the operation of logic gates has been performed independently without reconfiguration of the device structure, this paves the way for such devices to be an

integral part of logic circuits embedded within optical integrated chips with ultrahigh speed at low power level. Following similar concepts, the function of other logic gates and complex logic functions can also be realized by proper tuning of optical inputs and appropriate interconnections of such logic circuits.

Binary to decimal converter

In this section, we demonstrate the realization of converting a basic number system, binary to decimal, by employing the same device as in the previous section with an invariant structure. The 4 bit binary-to-decimal converter utilizes precisely tuned four optical inputs (385 nm, 490 nm, 595 nm, 740 nm) combinations (with each OPD of 2.0 mW cm⁻²) shown in Fig. 6a, considered as four binary inputs with 385 nm at the place of the most significant bit (MSB) and 740 nm at the place of the least significant bit (LSB). The optically induced electrical current output is regarded as equivalent decimal output (with some approximation). The device characteristics were measured in the dark and under exposure to selected wavelengths, as shown in Fig. S13.†

Fig. 6b represents the schematic diagram for the operation of the binary-to-decimal converter. A particular optical input represents a binary “1” when it is ON (used for exposure) and a binary “0” when it is OFF (not used for exposure). For binary input “0000”, all the optical inputs were set in the OFF

Table 2 Operational table for NAND gate, and NOR gate with 2-input binary combinations (optical) and logical output (resistance) showing a high (1) output if output resistance is higher than threshold (3.33 K Ω) and a low (0) output if output resistance is lower than threshold

V_{bg} (V)	Logic operation	Input-2 ($\lambda = 525$ nm) green	Input-1 ($\lambda = 635$ nm) red	Output resistance (K Ω)	Comparison with threshold resistance (3.33 K Ω)	Corresponding logical output
0	NAND	0	0	21.74	$21.74 > 3.33$	1
		0	1	3.82	$3.82 > 3.33$	1
		1	0	3.48	$3.48 > 3.33$	1
		1	1	3.15	$3.15 < 3.33$	0
10	NOR	0	0	10.41	$10.41 > 3.33$	1
		0	1	2.86	$2.86 < 3.33$	0
		1	0	2.72	$2.72 < 3.33$	0
		1	1	2.56	$2.56 < 3.33$	0



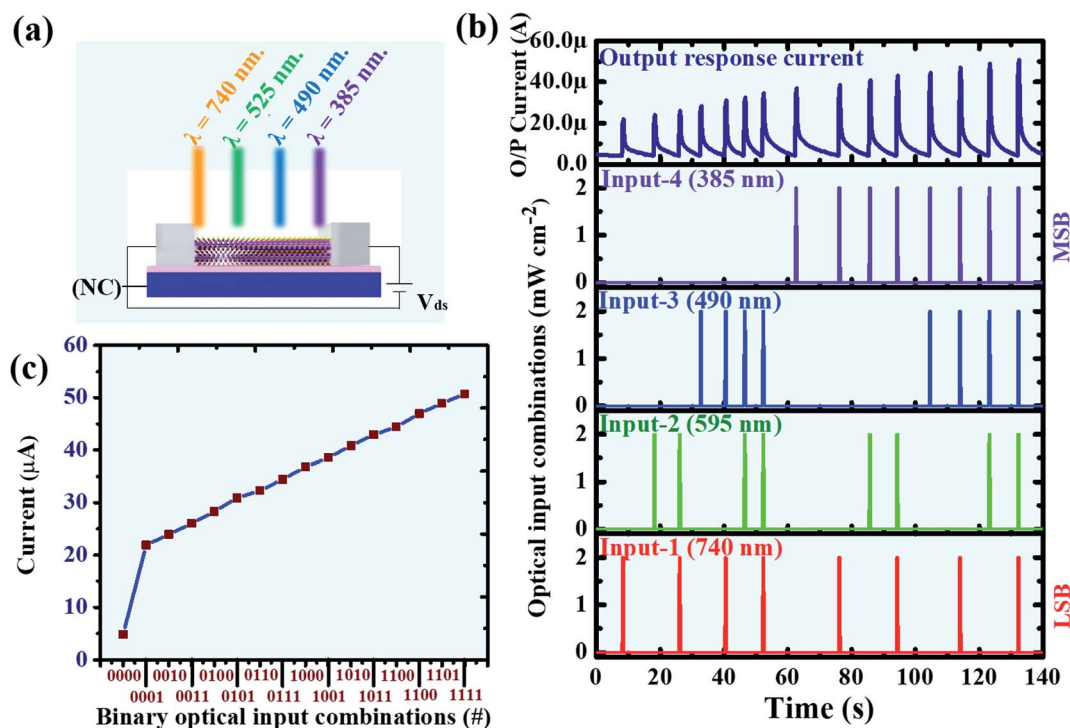


Fig. 6 Represents realization of binary to decimal conversion. (a) The device under exposure with wavelengths 740 nm, 595 nm, 490 nm, and 385 nm as binary optical inputs. (b) Represents device function by showing variation of output current in response to optical input combinations. (c) Linearity of output response current levels resulted from sequentially applying binary optical input combinations.

condition, and the output current was measured to be $4.86 \mu\text{A}$ (same as the dark current level). For binary input "0001", only wavelength 740 nm was applied for exposure, while other optical inputs remained in the OFF state. The measured output current was $21.89 \mu\text{A}$. Next, binary input combination 0010 was applied using a wavelength of 595 nm for exposure, keeping all other wavelengths in the OFF state. The measured output current was $23.94 \mu\text{A}$. The third binary input combination,

"0011", was applied using a wavelength of 740 nm and 595 nm for exposure while simultaneously maintaining other wavelengths in the OFF state. The output current was measured as $26.03 \mu\text{A}$. Following similar steps to apply optical inputs, all 4 bit binary input combinations from "0000" to "1111" were applied. The output current was measured to be $4.86 \mu\text{A}$, $21.89 \mu\text{A}$, $23.94 \mu\text{A}$, $26.03 \mu\text{A}$, $28.30 \mu\text{A}$, $30.91 \mu\text{A}$, $32.28 \mu\text{A}$, $34.43 \mu\text{A}$, $36.79 \mu\text{A}$, $38.54 \mu\text{A}$, $40.83 \mu\text{A}$, $42.95 \mu\text{A}$, $44.41 \mu\text{A}$, $46.97 \mu\text{A}$, $48.92 \mu\text{A}$

Table 3 Represents all optical combinations (with 740 nm, 595 nm, 490 nm, and 385 nm) as 4 bit binary inputs and their equivalent decimal output with intermediate approximations adopted

Input-4 ($\lambda = 385 \text{ nm}$)	Input-3 ($\lambda = 490 \text{ nm}$)	Input-2 ($\lambda = 595 \text{ nm}$)	Input-1 ($\lambda = 740 \text{ nm}$)	Output current level I_p (μA)	$d = (I_p - 20)/2$	$D = \text{Positive approximation of "d"}$
0	0	0	0	4.86	-7.57	0
0	0	0	1	21.89	0.945	1
0	0	1	0	23.94	1.97	2
0	0	1	1	26.03	3.015	3
0	1	0	0	28.30	4.15	4
0	1	0	1	30.91	5.455	5
0	1	1	0	32.28	6.14	6
0	1	1	1	34.43	7.215	7
1	0	0	0	36.79	8.395	8
1	0	0	1	38.54	9.27	9
1	0	1	0	40.83	10.415	10
1	0	1	1	42.92	11.46	11
1	1	0	0	44.41	12.205	12
1	1	0	1	46.97	13.485	13
1	1	1	0	48.92	14.46	14
1	1	1	1	50.73	15.365	15



μA , and $50.73 \mu\text{A}$, as represented in Table 3. The output current values show upgrading linear behavior (Fig. 6c) by leaving the first value $4.86 \mu\text{A}$ for input combination “0000”. The increment in output current was almost constant with an incremental difference of approximately $2 \mu\text{A}$ (with respect to peak values of current). We used an empirically fitted formula, $d = (I_p - 20)/2$ (where “ d ” is a reduced value with respect to the output peak current I_p for each binary optical input combination from “0000” to “1111”). This leads the output values to $-7.57, 0.945, 1.97, 3.015, 4.15, 5.455, 6.14, 7.215, 8.395, 9.27, 10.415, 11.46, 12.205, 13.485, 14.46,$ and 15.365 , respectively, as presented in Table 3. To visualize the equivalent decimal number from the output, the following empirically fitted formula was adopted, where “ D ” represents the equivalent decimal number, and “ a ” and “ b ” represent the integer and fractional parts of “ d ”, respectively.

$$D = \{0, d < 0\}$$

$$= \{a, d = a + b \text{ (} a = \text{integer part, } b = \text{fractional part} < 0.555)\}$$

$$= \{a + 1, d = a + b \text{ (} a = \text{integer part, } b = \text{fractional part} > 0.555)\}$$

By using this, the equivalent decimal output for input “0000” is “0” ($d = -7.57 < 0$), for input “0001”, the decimal output is “1” ($d = 0.945 = 0 + 0.945 > 0.555, D = a + 1 = 0 + 1 = 1$), for input “0010”, the decimal output is “2” ($d = 1.97 = 1 + 0.97 > 0.555, D = a + 1 = 1 + 1 = 2$), and for the following input combinations, the equivalent decimal output $D = “a”$ (as fractional part < 0.555). This leads to decimal values of 0, 1, 2, 3, 4, 5, 6, 7, 8, 9, 10, 11, 12, 13, 14, and 15, resulting from peak values of the output current corresponding to binary inputs from 0000 to 1111 (Table 3).

Therefore, the operation of a 4 bit binary-to-decimal converter has been demonstrated with the help of four different optical wavelengths that were precisely tuned to modulate the output current. This demonstration is a remarkable sign of the realization of interconversion among different number systems that can be applied for advanced computing.

Experimental section

Synthesis of $\text{Bi}_2\text{O}_2\text{Se}$ nanoplates over MICA substrate

A quartz tube (diameter = 3 inches) and an in-built LPCVD system composed of three different heating zones, T-1 (downstream), T-2 (middle), and T-3 (upstream), was adopted for the synthesis of $\text{Bi}_2\text{O}_2\text{Se}$ nanoplates. MICA as a suitable substrate was placed at the heating zone T-1, while precursors Bi_2O_3 and Bi_2Se_3 were placed at heating zones T-2 and T-3, respectively. To evacuate oxygen from the tube, a flow of Ar was used. The emblematic growth time was 40 min, with temperature conditions of $500 \text{ }^\circ\text{C}$, $700 \text{ }^\circ\text{C}$, and $500 \text{ }^\circ\text{C}$ for substrate (T-1), Bi_2O_3 (T-2), and Bi_2Se_3 (T-3), respectively, whereas the tube pressure was 100 torr and the flow rate of the carrier gas (Ar) was 200 sccm.

Material characterization

To capture optical microscopy (OM) images of $\text{Bi}_2\text{O}_2\text{Se}$ nanoplates, an optical microscope (OLYMPUS BX53 M) was used.

The thickness of $\text{Bi}_2\text{O}_2\text{Se}$ nanoplates was measured by atomic force microscopy (AFM B067, Bruker Corp.). Raman spectroscopy of the samples was carried out under excitation at 532 nm laser with a $100\times$ objective lens (UniDRON, CI Technology). The dimensions and elemental composition of $\text{Bi}_2\text{O}_2\text{Se}$ nanoplates were determined *via* FESEM analysis (JOEL JSM-7500F, accelerating voltage: 10 kV . Resolution: 1 nm) and EDS analysis (OXFORD INCA X-ACT), respectively. The cross-sectional HRTEM image of $\text{Bi}_2\text{O}_2\text{Se}$ was obtained *via* a focused-ion beam in a dual-beam microscope (JEM-2100F, acceleration voltage 200 kV).

Transferring $\text{Bi}_2\text{O}_2\text{Se}$ nanoplates from MICA to SiO_2 substrate

MICA (having as-grown $\text{Bi}_2\text{O}_2\text{Se}$ nanoplates) is first spin coated by PMMA in two steps (step-1: 500 rpm for 7 s , step-2: 2000 rpm for 60 s), then baked ($150 \text{ }^\circ\text{C}$, for 1 min) to improve the adhesion of PMMA with $\text{Bi}_2\text{O}_2\text{Se}$. A PDMS sheet of sufficient dimension was attached over the PMMA spin-coated substrate and baked again ($150 \text{ }^\circ\text{C}$ for 2 min) for better adhesion of the PDMS sheet. Cooling of the sample was done with a flow of N_2 . Next, water was used to separate the PDMS sheet from MICA by dipping the substrate in water for a sufficient period ($\sim 5 \text{ min}$). Due to good adhesion, $\text{Bi}_2\text{O}_2\text{Se}$ nanoplates remain attached to the PDMS sheet *via* the PMMA layer. This PDMS sheet was attached over fresh Si substrate (SiO_2/Si), baked ($150 \text{ }^\circ\text{C}$, for 2 min), and then cooled by N_2 . Acetone treatment helps to detach the PDMS sheet, leaving $\text{Bi}_2\text{O}_2\text{Se}$ nanoplates over the SiO_2/Si substrate. $\text{Bi}_2\text{O}_2\text{Se}/\text{SiO}_2/\text{Si}$ was treated many times with acetone/IPA to avoid the PMMA residue. The minimum PMMA residue was observed with samples kept in acetone overnight.

Device fabrication

For the fabrication of the device, an LED lithography system was used to define a 2-terminal pattern for metal contact by spin coating with PR AZ5214E in two steps (step-1: 700 rpm for 5 s , step-2: 4000 rpm for 60 s) followed by baking at $90 \text{ }^\circ\text{C}$ for 90 s . After exposure, an MIF-300 developer was used to develop the pattern (developer time was 4 s , water treatment was 20 s). The metal Pd (50 nm) was deposited by a thermal evaporator. Liftoff yields the two terminal patterns. Aluminum (Al, 3000 nm) was deposited to make the back contact using a thermal evaporator again.

Measurements

For both optical and electrical measurements simultaneously, a CoolLED pE-400 monochromatic light source ($\lambda = 365 \text{ nm} - 770 \text{ nm}$) was used with a semiconductor device analyzer B1500A. A NOVA II power meter (OPHIR Photonics) was utilized to measure the OPD (mW cm^{-2}). All measurements were completed in a sufficiently dark environment at room temperature.

Conclusion

In summary, we have demonstrated that a single $\text{Bi}_2\text{O}_2\text{Se}$ -based structure shows versatility for multiple optoelectronic



applications. The device performed the function of optoelectronic memory, starting with a write-in process done by trapping electrons generated by UV exposure, followed by achieving WT and read-out (detraping of electrons) by means of electrical energy. Furthermore, an associative learning process was demonstrated, controlled by a 635 nm optical wavelength (NS) and a 525 nm wavelength (US). The variation in the output current along the threshold level was used to discriminate the behavior (CR/UR). The same optical wavelengths are regarded as binary inputs to realize the operation of digital logic “AND”, “OR”, “NAND” and “NOR” gates. With the help of universal logic gates, the functions of other digital logic can be realized, creating a path for the development of low-power opto-digital logic devices. Moreover, four dissimilar wavelengths were observed: 740 nm, 595 nm, 490 nm, and 385 nm are precisely tuned and considered binary inputs for the implementation of a 4 bit binary to the decimal converter in which the value of the output current represents the equivalent decimal output. Our study elucidates the light sensing property of Bi₂O₂Se, making it a promising material for the development of in-computing optoelectronic memory, image sensor, and artificial intelligence.

Author contributions

Dharmendra Verma: conceptualization, data curation, investigation, methodology, writing – original draft. Bo Liu: validation, visualization, writing – review & editing. Tsung-Cheng Chen: validation, visualization, writing – review & editing. Lain-Jong Li: validation, writing – review & editing. Chao-Sung Lai: conceptualization, methodology, resources, validation, funding acquisition, project administration, supervision, writing – review & editing.

Conflicts of interest

The authors declare no conflict of interest.

Acknowledgements

The present study was supported by grants from the Ministry of Science and Technology (MOST), Taiwan (MOST 109-2221-E-182-013-MY3, MOST 110-2622-8-182-001-TS1) and Chang Gung Memorial Hospital, Taiwan (CMRPD2K0171).

References

- H. Tan, G. Liu, X. Zhu, H. Yang, B. Chen, X. Chen, J. Shang, W. D. Lu, Y. Wu and R.-W. Li, *Adv. Mater.*, 2015, **27**, 1500039.
- F. Zhou, Y. Liu, X. Shen, M. Wang, F. Yuan and Y. Chai, *Adv. Funct. Mater.*, 2018, **28**, 1800080.
- T. Leydecker, M. Herder, E. Pavlica, G. Bratina, S. Hecht, E. Orgiu and P. Samorì, *Nat. Nanotechnol.*, 2016, **11**, 769.
- J. Cheng, C. Wang, X. Zou and L. Liao, *Adv. Opt. Mater.*, 2018, **7**, 1800441.
- F. Zhou, J. Chen, X. Tao, X. Wang and Y. Chai, *Research*, 2019, 9490413.
- Z. Sun, J. Li, C. Liu, S. Yang and F. Yan, *Nano Lett.*, 2021, **21**, 723.
- T. Uda, A. Ishii and Y. K. Kato, *ACS Photonics*, 2018, **5**, 559.
- J. Zhao, Z. Wei, X. Yang, G. Zhang and Z. Wang, *Nano Energy*, 2020, **82**, 105692.
- C.-C. Shih, Y.-C. Chiang, H.-C. Hsieh, Y.-C. Lin and W.-C. Chen, *ACS Appl. Mater. Interfaces*, 2019, **11**, 42429.
- Y.-C. Chiang, C.-C. Hung, Y.-C. Lin, Y.-C. Chiu, T. Isono, T. Satoh and W.-C. Chen, *Adv. Mater.*, 2020, **32**, 2002638.
- X. Zhao, S.-Y. Wei, X.-H. Wang and L.-Z. Qiu, *Adv. Opt. Mater.*, 2021, **9**, 2002256.
- C. Gao, H. Yang, E. Li, Y. Yan, L. He, H. Chen, Z. Lin and T. Guo, *ACS Photonics*, 2021, **8**, 3094.
- L. Hu, J. Yuan, Y. Ren, Y. Wang, J.-Q. Yang, Y. Zhou, Y.-J. Zeng and S.-T. Han, *Adv. Mater.*, 2018, **30**, 1801232.
- M. D. Tran, H. Kim, J. S. Kim, M. H. Doan, T. K. Chau, Q. A. Vu, J.-H. Kim and Y. H. Lee, *Adv. Mater.*, 2018, **31**, 1807075.
- F. Gao, X. Zhang, B. Tan, S. Zhang, J. Zhang, D. Jia, Y. Zhou and P. A. Hu, *Small*, 2021, **17**, 2104459.
- Z. Cheng, C. Ríos, N. Youngblood, C. D. Wright, W. H. P. Pernice and H. Bhaskaran, *Adv. Mater.*, 2018, **30**, 1802435.
- I. Vassalini, I. Alessandri and D. Ceglie, *Materials*, 2021, **14**, 3396.
- M. S. Choi, G.-H. Lee, Y.-J. Yu, D.-Y. Lee, S. H. Lee, P. Kim, J. Hone and W. J. Yoo, *Nat. Commun.*, 2013, **4**, 1.
- D. Lee, E. Hwang, Y. Lee, Y. Choi, J. S. Kim, S. Lee and J. H. Cho, *Adv. Mater.*, 2016, **28**, 1603571.
- S. Lei, F. Wen, B. Li, Q. Wang, Y. Huang, Y. Gong, Y. He, P. Dong, J. Bellah, A. George, L. Ge, J. Lou, N. J. Halas, R. Vajtai and P. M. Ajayan, *Nano Lett.*, 2015, **15**, 259.
- K. Roy, M. Padmanabhan, S. Goswami, T. P. Sai, G. Ramalingam, S. Raghavan and A. Ghosh, *Nat. Nanotechnol.*, 2013, **8**, 826.
- J. Lee, S. Pak, Y.-W. Lee, Y. Cho, J. Hong, P. Giraud, H. S. Shin, S. M. Morris, J. I. Sohn, S. N. Cha and J. M. Kim, *Nat. Commun.*, 2013, **8**, 14734.
- A. Lipatov, N. S. Vorobeva, T. Li, A. Gruverman and A. Sinitskii, *Adv. Electron. Mater.*, 2021, **7**, 2001223.
- Y. Chen, J. Yu, F. Zhuge, Y. He, Q. Zhang, S. Yu, K. Liu, L. Li and Y. M. T. Zhai, *Mater. Horiz.*, 2020, **7**, 1331.
- K. Wang, J. Chen and X. Yan, *Nano Energy*, 2021, **79**, 105453.
- J. Zhao, Z. Zhou, H. Wang, J. Wang, W. Hao, D. Ren, R. Guo, J. Chen, B. Liu and X. Yan, *Appl. Phys. Lett.*, 2019, **115**, 153504.
- H. Chen, X. Xue, C. Liu, J. Fang, Z. Wang, J. Wang, D. W. Zhang, W. Hu and P. Zhou, *Nat. Electron.*, 2021, **4**, 399.
- K. Zhang, D. Meng, F. Bai, J. Zhai and Z. L. Wang, *Adv. Funct. Mater.*, 2020, **30**, 2002945.
- M. Pedraza, J. M. Martinez, R. Rodriguez, M. B. Gonzalez, F. Campabadal and M. Nafria, *Microelectron. Eng.*, 2019, **215**, 111024.
- M. Yan, Q. Zhu, S. Wang, Y. Ren, G. Feng, L. Liu, H. Peng, Y. He, J. Wang, P. Zhou, X. Meng, X. Tang, J. Chu, B. Dkhil, B. Tian and C. Duan, *Adv. Electron. Mater.*, 2021, **7**, 2001276.



- 31 Y. Pei, Z. Zhou, A. P. Chen, J. Chen and X. Yan, *Nanoscale*, 2020, **12**, 13531.
- 32 A. Emboras, A. Alabastri, P. Lehmann, K. Portner, C. Weilenmann, P. Ma, B. Cheng, M. Lewerenz, E. Passerini, U. Koch, J. Aeschlimann, F. Ducry, J. Leuthold and M. Luisier, *Appl. Phys. Lett.*, 2020, **117**, 230502.
- 33 J.-Y. Mao, L. Zhou, X. Zhu, Y. Zhou and S.-T. Han, *Adv. Optical Mater.*, 2019, **7**, 1900766.
- 34 Y. Wang, L. Yin, W. Huang, Y. Li, S. Huang, Y. Zhu, D. Yang and X. Pi, *Adv. Intell. Syst.*, 2021, **3**, 2000099.
- 35 J. Wu, C. Tan, Z. Tan, Y. Liu, J. Yin, W. Dang, M. Wang and H. Peng, *Nano Lett.*, 2017, **17**, 3021.
- 36 H. Fu, J. Wu, H. Peng and B. Yan, *Phys. Rev. B*, 2018, **97**, 241203.
- 37 J. Wu, Y. Liu, Z. Tan, C. Tan, J. Yin, T. Li, T. Tu and H. Peng, *Adv. Mater.*, 2017, **29**, 1704060.
- 38 J. Wu, C. Tan, Z. Tan, Y. Liu, J. Yin, W. Dang, M. Wang and H. Peng, *Nano Lett.*, 2017, **17**, 3021.
- 39 T. Ghosh, M. Samanta, A. Vasdev, K. Dolui, J. Ghatak, T. Das, G. Sheet and K. Biswas, *Nano Lett.*, 2019, **19**, 5703.
- 40 Y. Liang, Y. Chen, Y. Sun, S. Xu, J. Wu, C. Tan, X. Xu, H. Yuan, L. Yang, Y. Chen, P. Gao, J. Guo and H. Peng, *Adv. Mater.*, 2019, **31**, 1901964.
- 41 M.-Q. Li, L.-Y. Dang, G.-G. Wang, F. Li, M. Han, Z.-P. Wu, G.-Z. Li, Z. Liu and J.-C. Han, *Adv. Mater. Technol.*, 2020, **5**, 2000180.
- 42 Y. Sun, S. Ye, J. Zhang, J. Song, F. Zhou and J. Qu, *J. Mater. Chem. C*, 2020, **8**, 14711.
- 43 C. Zhang, J. Wu, Y. Sun, C. Tan, T. Li, T. Tu, Y. Zhang, Y. Liang, X. Zhou, P. Gao and H. Peng, *J. Am. Chem. Soc.*, 2020, **142**, 2726.
- 44 M. Kang, H.-J. Chai, H. B. Jeong, C. Park, I.-Y. Jung, E. Park, M. M. Çiçek, I. Lee, B.-S. Bae, E. Durgun, J. Y. Kwak, S. Song, S.-Y. Choi, H. Y. Jeong and K. Kang, *ACS Nano*, 2021, **15**, 8715.
- 45 U. Khan, Y. Luo, L. Tang, C. Teng, J. Liu, B. Liu and H.-M. Cheng, *Adv. Funct. Mater.*, 2019, **29**, 1807979.
- 46 T. Selvamani, S. Anandan, L. Granone, D. W. Bahnemann and M. Ashokkumar, *Mater. Chem. Front.*, 2018, **2**, 1664.
- 47 C. Tan, M. Tang, J. Wu, Y. Liu, T. Li, Y. Liang, B. Deng, Z. Tan, T. Tu, Y. Zhang, C. Liu, J.-H. Chen, Y. Wang and H. Peng, *Nano Lett.*, 2019, **19**, 2148.
- 48 M. Wu and X. C. Zeng, *Nano Lett.*, 2017, **17**, 6309.
- 49 H. Yang, C. Tan, C. Deng, R. Zhang, X. Zheng, X. Zhang, Y. Hu, X. Guo, G. Wang, T. Jiang, Y. Zhang, G. Peng, H. Peng, X. Zhang and S. Qin, *Small*, 2019, **15**, 1904482.
- 50 A. L. J. Pereira, D. Santamaria-Pérez, J. Ruiz-Fuertes, F. J. Manjón, V. P. Cuenca-Gotor, R. Vilaplana, O. Gomis, C. Popescu, A. Muñoz, P. Rodríguez-Hernández, A. Segura, L. Gracia, A. Beltrán, P. Ruleova, C. Drasar and J. A. Sans, *J. Phys. Chem. C*, 2018, **122**, 8853.
- 51 Q. Fu, C. Zhu, X. Zhao, X. Wang, A. Chaturvedi, C. Zhu, X. Wang, Q. Zeng, J. Zhou, F. Liu, B. K. Tay, H. Zhang, S. J. Pennycook and Z. Liu, *Adv. Mater.*, 2018, **31**, 1804945.
- 52 J. Wu, C. Qiu, H. Fu, S. Chen, C. Zhang, Z. Dou, C. Tan, T. Tu, T. Li, Y. Zhang, Z. Zhang, L.-M. Peng, P. Gao, B. Yan and H. Peng, *Nano Lett.*, 2019, **19**, 197.
- 53 J. Li, Z. Wang, Y. Wen, J. Chu, L. Yin, R. Cheng, L. Lei, P. He, C. Jiang, L. Feng and J. He, *Adv. Funct. Mater.*, 2018, **28**, 1706437.
- 54 J. Yang, R. Quhe, Q. Li, S. Liu, L. Xu, Y. Pan, H. Zhang, X. Zhang, J. Li, J. Yan, B. Shi, H. Pang, L. Xu, Z. Zhang, J. Lu and J. Yang, *Adv. Electron. Mater.*, 2019, **5**, 1800720.
- 55 R. Quhe, J. Liu, J. Wu, J. Yang, Y. Wang, Q. Li, T. Li, Y. Guo, J. Yang, H. Peng, M. Lei and J. Lu, *Nanoscale*, 2019, **11**, 532.
- 56 C. Huang and H. Yu, *ACS Appl. Mater. Interfaces*, 2020, **12**, 19643.
- 57 Y. Chen, W. Ma, C. Tan, M. Luo, W. Zhou, N. Yao, H. Wang, L. Zhang, T. Xu, T. Tong, Y. Zhou, Y. Xu, C. Yu, C. Shan, H. Peng, F. Yue, P. Wang, Z. Huang and W. Hu, *Adv. Funct. Mater.*, 2021, **31**, 2009554.
- 58 J.-M. Yan, J.-S. Ying, M.-Y. Yan, Z.-C. Wang, S.-S. Li, T.-W. Chen, G.-Y. Gao, F. Liao, H.-S. Luo, T. Zhang, Y. Chai and R.-K. Zheng, *Adv. Funct. Mater.*, 2021, **31**, 2103982.
- 59 B. Liu, Y. Zhao, D. Verma, L. A. Wang, H. Liang, H. Zhu, L.-J. Li, T.-H. Hou and C.-S. Lai, *ACS Appl. Mater. Interfaces*, 2021, **13**, 15391.
- 60 J. Wu, H. Yuan, M. Meng, C. Chen, Y. Sun, Z. Chen, W. Dang, C. Tan, Y. Liu, J. Yin, Y. Zhou, S. Huang, H. Q. Xu, Y. Cui, H. Y. Hwang, Z. Liu, Y. Chen, B. Yan and H. Peng, *Nat. Nanotechnol.*, 2017, **12**, 530.
- 61 C. Tan, S. Xu, Z. Tan, L. Sun, J. Wu, T. Li and H. Peng, *InfoMat*, 2019, **1**, 390.
- 62 C.-M. Yang, T.-C. Chen, D. Verma, L.-J. Li, B. Liu, W.-H. Chang and C.-S. Lai, *Adv. Funct. Mater.*, 2020, **30**, 2001598.
- 63 M. Yu, C. Fang, J. Han, W. Liu, S. Gao and K. Huang, *ACS Appl. Mater. Interfaces*, 2022, **14**, 13507.
- 64 S. Yang, P. Luo, F. Wang, T. Liu, Y. Zhao, Y. Ma, H. Li and T. Zhai, *Small*, 2022, **18**, 2105211.
- 65 S. Liu, D. He, C. Tan, S. Fu, X. Han, M. Huang, Q. Miao, X. Zhang, Y. Wang, H. Peng and H. Zhao, *Small*, 2022, **18**, 2106078.
- 66 C. Fan, B. Dai, H. Liang, X. Xu, Z. Qi, H. Jiang, H. Duan and Q. Zhang, *Adv. Funct. Mater.*, 2021, **31**, 2010263.
- 67 W. Chen, U. Khan, S. Feng, B. Ding, X. Xu and B. Liu, *Adv. Funct. Mater.*, 2020, **30**, 2004960, (Ref. added in manuscript with no. = 20).
- 68 Y. Guo, X. Wei, J. Shu, B. Liu, J. Yin, C. Guan, Y. Han, S. Gao and Q. Chen, *Appl. Phys. Lett.*, 2015, **106**, 103109.
- 69 M. S. Fanselow and A. M. Poulos, *Annu. Rev. Psychol.*, 2005, **56**, 207.

